PHYSICAL REVIEW C **104**, 034315 (2021)

Nuclear matter density distributions of the neutron-rich ^{6,8}He isotopes from a sum-of-Gaussian analysis of elastic proton scattering data at intermediate energies

X. Liu,[1,2,*] P. Egelhof,[2] O. Kiselev,[2] and M. Mutterer[2,†]

[1] *Key Laboratory of Radiation Physics and Technology of the Ministry of Education, Sichuan University, Chengdu 610064, China*
[2] *GSI Helmholtzzentrum für Schwerionenforschung GmbH, 64291 Darmstadt, Germany*

(Received 14 June 2021; accepted 1 September 2021; published 17 September 2021)

Differential cross sections for elastic p-^{6}He and p-^{8}He scattering, measured in inverse kinematics at high momentum transfer up to the first diffraction minimum and at projectile energies around 700 MeV/u at GSI Darmstadt, are analyzed applying the sum-of-Gaussians (SOG) method based on the Glauber multiple-scattering theory. The rms point matter radii of ^{6}He and ^{8}He are deduced to be 2.29(6) fm and 2.53(7) fm, respectively, in close agreement with those from former analyses using phenomenological parametrizations for describing the matter distributions. With the aid of the measurement at high momentum transfer, the overall radial density distributions of ^{6}He and ^{8}He are precisely deduced using the SOG method, in particular at small radii. A pronounced core rearrangement by adding the valence neutrons to an α-like core to form ^{6}He and ^{8}He is elucidated, and briefly discussed.

DOI: 10.1103/PhysRevC.104.034315

I. INTRODUCTION

During the past three decades there has been a growing interest in the structure of neutron-rich light nuclei near the dripline. As fundamental properties, their size and the radial density distribution of nuclear matter provide one of the most reliable ways of understanding nuclear structure in light unstable nuclei, in particular the halo structure, which exhibits an extended distribution of the valence neutrons surrounding a compact core [1–5]. Over the years a large variety of experimental methods have been developed for exploring the nuclear matter distributions of the stable nuclei [6–10]. Among them, intermediate-energy (≈500 MeV to 1 GeV) elastic scattering of hadronic probes, predominantly protons and α particles, has early become a powerful technique and has been applied over a wide mass range of nuclei [10–15]. This method was further improved, and for the first time applied at GSI Darmstadt for investigating the nuclear matter distributions in light unstable nuclei using the technique of inverse kinematics [3,16–22]. The first experiment of this kind, described in detail elsewhere [17,18], was performed using the radioactive beams of ^{6,8}He with incident energies around 700 MeV/u from the FRagment Separator (FRS) of GSI to irradiate the hydrogen-filled active target IKAR which simultaneously served as a gas target and a detector for the recoil protons. For comparison, elastic proton scattering from the stable ^{4}He nucleus was measured under the same conditions. The absolute differential cross sections $d\sigma/dt$ for the elastic proton scattering from the ^{4,6,8}He nuclei as a function of the Lorentz-invariant four-momentum transfer squared $-t$ were measured in the region of low momentum transfer $0.002 \leqslant |t| \leqslant 0.05$ (GeV/c)^2. Later, the matter root-mean-square (rms) radii R_m and radial matter density distributions of ^{4,6,8}He were deduced [23] by analyzing the measured differential cross sections using the Glauber multiple-scattering theory [24]. Nevertheless, although theoretical calculations have shown that the elastic proton scattering measurement at low momentum transfer is sensitive to the nuclear matter density at the nuclear periphery, allowing us to deduce the nuclear size precisely [23], investigations at higher momentum transfer are necessary to explore the densities of the interior nuclear matter [25,26]. The elastic proton scattering measurement at higher momentum transfer is therefore of great importance to improve the accuracy of the determination of the overall nuclear matter distributions in the ^{6,8}He and other nuclei.

For this purpose, an additional experiment was later accomplished at GSI Darmstadt with the aim to measure the p-^{6,8}He differential cross sections at higher momentum transfer close to the first diffraction minimum [19,27]. The major difference with respect to the previous experiment was that instead of using the active gaseous target, a liquid hydrogen target was used for the elastic p-^{6,8}He scattering experiment, combined with a proton recoil detector. In that experiment, $d\sigma/dt$ at a momentum transfer range, $0.05 \leqslant |t| \lesssim 0.2$ (GeV/c)^2, was successfully measured. To deduce the matter radii and radial density distributions of ^{6,8}He, the combined data set of the elastic p-^{6,8}He scattering cross sections measured at both low and high momentum transfer, $0.002 \leqslant -t \lesssim 0.2$ (GeV/c)^2, was analyzed using the Glauber multiple-scattering theory with the spin-orbital interaction explicitly taken into account [28]. An enhanced sensitivity of the data measured at high momentum transfer to the α-like core region of the ^{6,8}He densities was found, demonstrating the important role of the data determined at high momentum transfer for deducing the shapes of the core of the radial matter distributions in light halo nuclei [28]. However, a drawback in

---

[*] Corresponding author: liuxingquan@scu.edu.cn

[†] Deceased.

the analysis described in Ref. [28] arises from the application of phenomenological model parametrizations for describing the nuclear matter densities, such as the symmetrized Fermi, Gaussian-halo, and Woods-Saxon distributions, as it makes local density properties hard to derive [29]. The deduced matter densities of ^{6,8}He are therefore significantly dependent on the selection of particular density parametrizations. A similar drawback exists in the previous analysis of Alkhazov *et al.* [23] as well, although a series of different phenomenological model functions were applied allowing for reducing the model dependence, and the variation of the results was used as indicator for the systematic uncertainty.

Recently, a sum-of-Gaussians (SOG) method was applied [30] to analyze the elastic proton scattering data of self-conjugate doubly magic radioactive ^{56}Ni and stable ^{58}Ni measured in inverse kinematics at the Experimental Storage Ring (ESR) at GSI Darmstadt in the frame of the EXL project [31–33]. The SOG method [29] has been successfully applied for many years for deducing nuclear charge distributions from electron scattering data [34]. The matter radii and radial density distributions of ^{56,58}Ni were deduced using this method, and a pronounced difference in the deduced matter distributions between both nuclei was observed for the first time [30]. It was demonstrated in this work that although there is close agreement of the matter radii deduced using phenomenological parametrizations for modeling the nuclear matter distributions, the matter density distributions from the SOG method provide more abundant information on the nuclear structure, and only the SOG method is capable of elucidating the characteristic difference in the radial distribution of nuclear matter [30]. In the present article, we use the SOG method, which is supposed to produce, as compared to the use of phenomenological parametrizations for modeling the nuclear matter distributions, less model-dependent results, to analyze the combined cross section data of elastic p-^{6,8}He scattering at both low and high momentum transfer [18,19] for deducing the matter rms radii and matter density distributions of ^{6}He and ^{8}He. The SOG method used in the analysis on ^{56,58}Ni is improved for permitting the applicability of the SOG method for nuclei with extended nuclear matter distributions such as expected for ^{6,8}He.

II. SUM-OF-GAUSSIANS METHOD

In the SOG method, the nuclear matter density distribution for a given atomic nucleus is deduced by fitting the measured differential cross sections of elastic p nucleus scattering within the framework of the Glauber multiple-scattering theory [24]. For the case of a compact nucleus, the nuclear matter density distribution $\rho(r)$, similar to the previous SOG analysis of the ^{56,58}Ni nuclei [30], is described by a summation of multi-Gaussian functions at arbitrary radii r_i ($r_i \in [0, R_{\max}]$ fm) with arbitrary amplitudes A_i as in Ref. [29],

$$\rho(r) = \frac{1}{2\pi^{3/2}\gamma^3} \sum_{i}^{N_g} \frac{A_i}{1 + 2r_i^2/\gamma^2} \times \left(\exp\left[-\frac{(r - r_i)^2}{\gamma^2}\right] + \exp\left[-\frac{(r + r_i)^2}{\gamma^2}\right]\right), \quad (1)$$

where γ is the common width of the Gaussians and N_g is the total number of Gaussians. γ, N_g, and $R_{\max}$ are basic inputs for establishing the given $\rho(r)$, and r_i and A_i are the free fitting parameters. To eliminate the model-dependent effect by introducing the parametrizations of γ, $R_{\max}$, and N_g (if any), reasonably good physical arguments have been addressed [30]. The formalism of the SOG density in Eq. (1) was originally used for studying the charge density distributions of stable nuclei [29]. In contrast to the ^{56,58}Ni nuclei, in which no significant extended tail structure is found at large radii [30], it is well known that the presently investigated ^{6,8}He nuclei exhibit pronounced tail structures with widely extended distributions at large radii. Therefore, specific constraints for the selection of γ and $R_{\max}$ in the SOG density should be taken into account as compared to those already used in Ref. [30].

Theoretical calculations [35,36] show that in ^{6}He and ^{8}He, the radial wave functions for describing the extended matter distributions have generally a width around two times that for the core. This indication is well evidenced by the experimental analysis of the combined p-^{6,8}He scattering cross section data using the Gaussian-Gaussian and Gaussian-oscillator parametrizations for the matter densities, that the obtained halo radius R_h is nearly two times that of the core radius R_c for both ^{6,8}He nuclei [28], where R_c and R_h are for describing the core and halo densities, respectively. To take this into account, different γ values for the core and the halo in ^{6,8}He are used in Eq. (1). The γ for describing the α-like core region of ^{6,8}He (denoted as γ_c) is taken around 1.0 fm, limited by the finite nucleon size (≈0.9 fm) and the smallest oscillatory structure from the various theoretical calculations (≈1.1 fm), similar to that in Ref. [37]. In contrast, the γ for the halo region (denoted as γ_h) is taken as two times that of γ_c. For defining the regions of core and halo, a parameter for quantifying the rms distance from the core center to the valence neutrons, R_{c-h}, is used. The value of R_{c-h} for ^{6}He has been experimentally deduced to be 3.84(6) fm with the aid of a geometrical model [2]. Therefore, a value of $R_{c-h} = 4$ fm is taken for ^{6,8}He for the present analysis. In the following SOG analysis, R_{c-h} is further randomly varied in the range from 4 to 5 fm to reduce the model dependence. Due to the widely extended distribution of the loosely bound valence neutrons in ^{6,8}He, the matter density distributions of ^{6,8}He both decrease slowly at large radii. Therefore, a large $R_{\max}$ value of 12 fm is taken. N_g is chosen to be bigger than 12, based on the criterium of $N_g > R_{\max}/\gamma_c$.

In Ref. [23], it was found that the experimental cross sections even at extremely low momentum transfer are not sensitive to the far periphery part of the nucleus with a pronounced tail structure, so that additional information on the asymptotic density behavior at large radii, for example that from theoretical predictions [38], has to be taken into account to reduce the uncertainties in deducing the matter distributions at the nuclear periphery due to the weak constraint from the low momentum transfer data. In the present SOG analysis, in addition to the experimental data, the asymptotic density behavior at far peripheral regions predicted by two theoretical calculations is introduced to supplement the SOG fits. Following the treatment in Ref. [23], for the ^{6}He nucleus, the far periphery density calculated from a representative wave

TABLE I. Parameters γ_c, γ_h, R_{c-h}, $R_{\max}$, and N_g for establishing the SOG densities of ^{6}He and ^{8}He, and wave functions for constraining their extended tails. Note that in the SOG analysis, γ_c, γ_h, and N_g are randomly varied around the values given in the table, i.e., $\gamma_c \in [0.9, 1.1]$ fm, $\gamma_h \in [1.8, 2.2]$ fm, and $N_g \in [20, 30]$, for permitting a larger variability of the shape of the density distribution.

Nucleus	γ_c (fm)	γ_h (fm)	R_{c-h} (fm)	$R_{\max}$ (fm)	N_g	Tail function
^{6}He	1.0	2.0	[4.0, 5.0]	12.0	>12	FC [38]
^{8}He	1.0	2.0	[4.0, 5.0]	12.0	>12	Hankel [40]

function model using a three-body wave function with three Faddeev components (the FC wave function) tabulated in Ref. [39] is adopted, and for the ^{8}He nucleus, the far periphery density is adopted as a square of a spherical Hankel wave function [40] assuming the one-neutron separation energy to be 2.59 MeV, a summation of the two-neutron separation energy, 2.14 MeV, and the energy of the resonant state of the residual ^{7}He, 0.45 MeV (see also Ref. [23]). Here, the asymptotic density selection from the FC and Hankel wave functions for constraining the ^{6,8}He tail structures is somewhat "arbitrary," but reasonably good physical arguments have been addressed in Refs. [23,38], that by using the FC wave function, one is able to well reproduce the present elastic p-^{6}He scattering cross section data at low momentum transfer, and it is also the wave function calculation with the FC wave function that provides the best description of the empirical two-neutron separation energy of 0.97 MeV, and that the periphery asymptotic density behavior from the Hankel wave function for ^{8}He describes quite well the shape of the periphery tail of the nuclei with four valence nucleons [20,38]. Moreover, as described below, the theoretical wave functions are plugged in the present SOG analysis with large uncertainties to weaken the model-dependent effect, if any. The parametrizations of γ_c, γ_h, R_{c-h}, $R_{\max}$, and N_g for establishing the SOG densities of ^{6}He and ^{8}He, and the wave functions chosen for constraining their extended tails, are summarized in Table I. For further permitting a larger variability of the shape of the density distribution, γ_c, γ_h, and N_g are randomly varied in the following SOG analysis (see below).

In the Glauber multiple-scattering theory [24], the relation between the differential cross section $d\sigma/dt$ for elastic proton scattering and the elastic p-nucleus scattering amplitude, $F_{el}(\mathbf{q})$, is given by [12,24]

$$\frac{d\sigma}{dt} = \frac{\pi}{k^2}|F_{el}(\mathbf{q})|^2, \tag{2}$$

with

$$F_{el} = \frac{ik}{2\pi}\int e^{i\mathbf{qb}}\left\{1-\prod_{i}^{A}[1-\gamma_{pN}(\mathbf{b}-\mathbf{s}_i)]\right\} \times \rho_A(\mathbf{r}_1,\mathbf{r}_2,\ldots,\mathbf{r}_A)d^3\mathbf{r}_1 d^3\mathbf{r}_2\ldots d^3\mathbf{r}_A d^2\mathbf{b}. \tag{3}$$

Here, $\mathbf{q}$ is the momentum transfer, k is the wave number of the incident proton, $\mathbf{b}$ is the impact vector, A is the nuclear mass number, and $\rho_A(\mathbf{r}_1,\mathbf{r}_2,\ldots,\mathbf{r}_A)$ is the density product, $\rho_A(\mathbf{r}_1,\mathbf{r}_2,\ldots,\mathbf{r}_A)=\prod_{i=1}^{A}\rho_i(\mathbf{r}_i)$, where $\rho_i(\mathbf{r}_i)$ is the density at a given $\mathbf{r}_i$ for the ith nucleon. The center-of-mass correlations, arising due to the requirement that all nucleon radius vectors $\mathbf{r}_i$ have to sum-up to zero, have been taken into account following Ref. [12]. In practice, the $\rho_A(\mathbf{r}_1,\mathbf{r}_2,\ldots,\mathbf{r}_A)$ is given by the product, $\rho_A(\mathbf{r}_1,\mathbf{r}_2,\ldots,\mathbf{r}_A)=\prod_{i=1}^{A}\rho(\mathbf{r}_i)$, where $\rho(\mathbf{r}_i)$ is the density at a given $\mathbf{r}_i$ deduced using the identical one-body nucleon distribution $\rho(r)$ defined by Eq. (1) without distinguishing between neutrons and protons. $\gamma_{pN}(\mathbf{b}-\mathbf{s}_i)$ represents the ith profile function for the pairwise proton-nucleon (pN) interactions, where $\mathbf{s}_i$ is the ith transverse nucleon coordinate. The profile function $\gamma_{pN}(\mathbf{b})$ can be related to the corresponding pN scattering amplitude $f_{pN}(\mathbf{q})$ of pN scattering as

$$\gamma_{pN}(\mathbf{b}) = \frac{1}{2i\pi k}\int e^{-i\mathbf{qb}}f_{pN}(\mathbf{q})d^2\mathbf{q}. \tag{4}$$

Following Ref. [12], only the scalar part of the elementary pN scattering amplitude is taken into account, and is described by the standard high-energy parametrization with the total pN cross sections (σ_{pN}), the ratios of the real to the imaginary parts of the pN amplitudes (ϵ_{pN}), and the slope parameters (β_{pN}) as

$$f_{pN}(\mathbf{q}) = \frac{ik}{4\pi}\sigma_{pN}(1-i\epsilon_{pN})\exp\left(-\frac{\mathbf{q}^2\beta_{pN}}{2}\right). \tag{5}$$

For avoiding implementation of some model dependence via the scattering amplitudes and for improving the accuracy of the Glauber calculations, experimental values of σ_{pN}, ϵ_{pN}, and β_{pN} at given incident energies are adopted in Eq. (5). For the present analysis, σ_{pN} and ϵ_{pN} at energies of 717 and 671 MeV/u for elastic p-^{6}He and ^{8}He scattering are evaluated by MINUIT polynomial fits to the data from the Particle Data Group (PDG) [41] and Refs. [23,42], respectively. The resulting σ_{pN} and ϵ_{pN} values are listed in Table II. The uncertainties of σ_{pN} and ϵ_{pN} are the fitting errors. Unlike σ_{pN} and ϵ_{pN}, the experimental data of the slope parameter β_{pN} are rather scarce. Therefore, the β_{pN} values are adjusted to give the best SOG description of the measured p-^{4}He cross section at around 700 MeV/u [18,43] with the known radius under the assumption of $\beta_{pp}=\beta_{pn}$ [23]. As the charge rms radius of ^{4}He has been precisely deduced to be 1.681(4) fm by analyzing the elastic e-^{4}He scattering data using a model-independent SOG method [44], and the neutrons and protons distribute equally in ^{4}He, the charge radius of ^{4}He is taken as reference. For the stable ^{4}He, the original SOG density formalism for the previous SOG analysis of ^{56,58}Ni nuclei is used [30], where γ is taken as 1.0 fm similar to that of Ref. [37]; $R_{\max}=5$ fm is taken from the independent knowledge on the behavior of wave functions, that the ^{4}He densities at radii greater than 5 fm decrease rapidly and have a negligible contribution; $N_g > 5$ is limited satisfying the criterion of $N_g > R_{\max}/\gamma$.

TABLE II. pN scattering amplitude parameters, σ_{pN}, ϵ_{pN}, and β_{pN}, used for the present SOG analysis of elastic p-^{6,8}He scattering.

Reaction	E_{inc} (MeV/u)	σ_{pp} (mb)	σ_{pn} (mb)	ϵ_{pp}	ϵ_{pn}	β_{pN} (fm^2)
p-^{6}He	717	43.5(1.6)	37.4(1.8)	0.094(41)	−0.299(42)	0.183(5)
p-^{8}He	671	41.4(1.5)	36.7(1.6)	0.132(40)	−0.269(42)	0.183(5)

The experimental pN scattering amplitude parameters σ_{pN} and ϵ_{pN} at 700 MeV are obtained from the fits to the experimental data as $\sigma_{pp} = 42.8(1.5)$ mb, $\sigma_{pn} = 37.2(1.8)$ mb, and $\epsilon_{pp} = 0.108(41)$, $\epsilon_{pn} = -0.289(42)$. With the selected values for γ, $R_{\max}$, and N_g, and the obtained pN scattering amplitude parameters, the free parameters of r_i and A_i can be deduced by a least-squares fit of the calculated to the measured cross sections of elastic p-^{4}He scattering using the SOG method. To reduce the number of parameters, r_i is first randomly distributed within 0–5 fm for each fit. Ten thousand individual SOG fits are performed. During the fits, γ and N_g are randomly varied, i.e., $\gamma \in [0.9, 1.1]$ fm, and $N_g \in [6, 12]$. The pN scattering amplitude parameters, σ_{pN} and ϵ_{pN}, are also randomly determined within their experimental uncertainties, and β_{pN} is randomly taken within 0.1–0.3 fm^2. Following the method described in Ref. [30], the χ^2 for the quality of the fits is defined as

$$\chi^2 = \sum_j^2 \sum_i^{N_j} \left\{ \left[\frac{\frac{d\sigma_{exp}}{dt}\big|_{t_i} - \left(\frac{d\sigma_{SOG}}{dt}\big|_{t_i}\right)/A_{Nor,j}}{\Delta\left(\frac{d\sigma_{exp}}{dt}\big|_{t_i}\right)} \right]^2 + \left(\frac{1-A_{Nor,j}}{\Delta A_{exp,j}}\right)^2 \right\}, \tag{6}$$

where $j = 1, 2$ corresponds to two elastic p-^{4}He scattering data sets taken from Refs. [18,43]. N_j is the data point number for the jth data set. $\frac{d\sigma_{exp}}{dt}|_{t_i}$ and $\Delta\frac{d\sigma_{exp}}{dt}|_{t_i}$ are the experimental cross section and its error at a certain momentum transfer t_i, respectively; $\frac{d\sigma_{SOG}}{dt}|_{t_i}$ is the calculated cross section at the same t_i. $A_{Nor,j}$ is the normalization factor of the calculated results to the experimental data for the jth data set, and $\Delta A_{exp,j}$ is the uncertainty in the experimental absolute normalization. ΔA_{exp} for both data sets has been commonly deduced as 3% in Refs. [18,43]. From the SOG fits, the resulting χ^2 distributes from around 70 to several thousand, corresponding to the quality of the experimental data. As demonstrated in the inset of Fig. 1, the χ^2 forms a sharp peak at the lowest value side of the χ^2 probability histogram. Good fits are selected with $\chi^2 < 80$, allowing for selecting out the fits with the minimum χ^2 values. The same criteria are also applied for the good fit selection in the ^{6,8}He analyses below. All selected fits are presented as a bundle of solid lines in Fig. 1. The measured cross sections are described by these fits rather well as observed in the figure. Each fit contributing to the bundle corresponds to one unique point matter rms radius and one point matter density distribution of ^{4}He. Folding the resulting point matter rms radius with the proton size, the folded matter rms radius, R_m^{folded}, is deduced, and plotted as a function of the input slope parameter β_{pN} in Fig. 2. A rather linear relation between R_m^{folded} and β_{pN} is obtained. Using the precisely deduced ^{4}He charge radius of 1.681(4) fm as reference by the dashed horizontal area, the corresponding β_{pN} is obtained via projection as $\beta_{pN} = 0.183(5)$ fm^2, where the error is indicated by the dashed vertical area. Using this deduced effective β_{pN} value is considered to account, to some extent, for the spin effect which has not been explicitly treated in the present Glauber calculations [12,23]. The point radial matter density distribution of ^{4}He deduced in the present analysis with $\beta_{pN} = 0.183(5)$ fm^2 is plotted in Fig. 3, where the shaded bands in the figure represent the uncertainties at given radii. For a cross-check, the obtained ^{4}He point matter density distribution is folded with the proton size, and compared with an available radial charge density obtained from the earlier model-independent analysis of elastic e-^{4}He scattering using the SOG method which gives a charge radius of 1.676(8) fm [34] in the figure, where the radial charge density has been normalized to the mass number of the ^{4}He nucleus. A rather good agreement for both the folded matter density and the normalized charge density is achieved within errors. It proves a good precision and an applicability of the present SOG method.

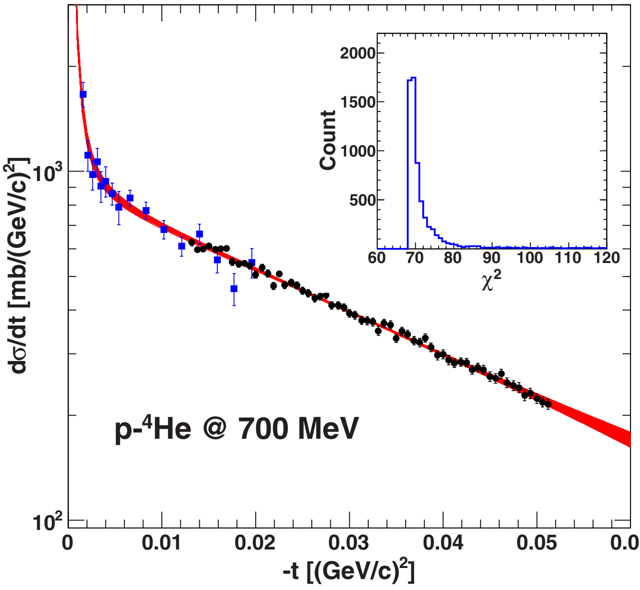

FIG. 1. Measured differential cross section $d\sigma/dt$ as a function of the four-momentum transfer squared $-t$ for elastic p-^{4}He scattering at 700 MeV/u. Squares and dots represent the data taken from Refs. [43] and [18], respectively. The bundle of solid lines corresponds to all "good" fits within the framework of the Glauber multiple-scattering theory using SOG distributions for describing the matter densities. The inset shows the probability histogram of the resulting χ^2 values from the SOG fits.

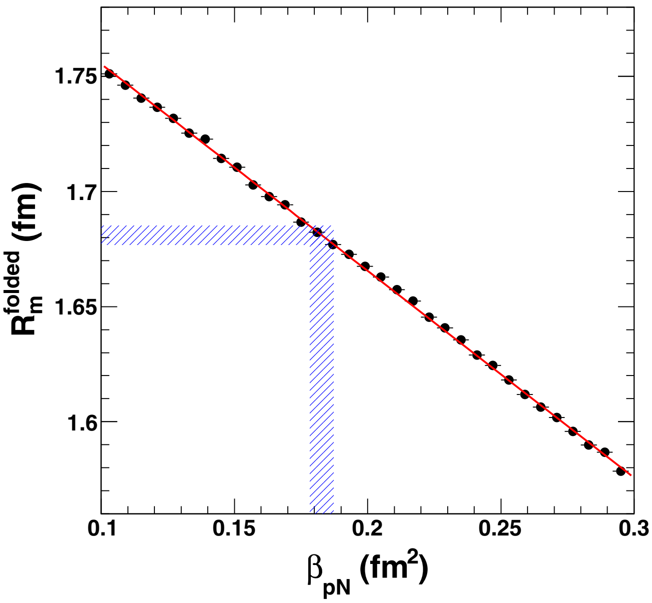

FIG. 2. Folded nuclear matter rms radius R_m^{folded} of ^{4}He as a function of input slope parameter β_{pN}. The red solid line is the linear fit to the resulting points. The blue dashed horizontal area indicates the charge rms radius of ^{4}He, 1.681(4) fm, deduced by analyzing the elastic e-^{4}He scattering data using the model-independent SOG method [44]. The dashed vertical area marks the β_{pN} region corresponding to the known charge rms radius.

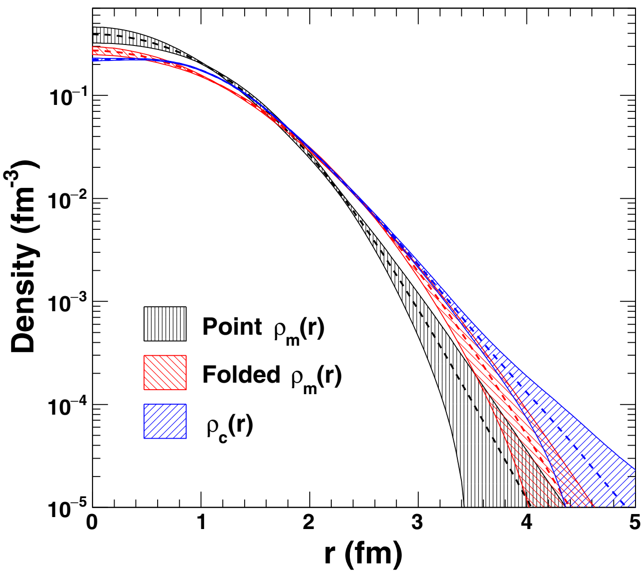

FIG. 3. The point nuclear matter density distribution of p-^{4}He deduced from the present SOG analysis of the experimental cross section of elastic p-^{4}He scattering with $\beta_{pN} = 0.183(5)$ fm^2 (in black) is compared with the folded matter density distribution (in red), and the radial charge density $\rho_c(r)$ obtained from a model-independent analysis of elastic e-^{4}He scattering using the SOG method which gives a charge radius of 1.676(8) fm [34] (in blue). The radial charge density has been normalized to the mass number of the ^{4}He nucleus. The dashed lines represent the mean distributions, and the shaded error bands relate to the errors from the standard deviation at given radii.

III. RESULTS AND DISCUSSION

Using the parameters listed in Tables I and II, more than ten thousand SOG fits are performed for the elastic p-^{6,8}He scattering cross sections. Similar to the case of ^{4}He, r_i is randomly distributed within $[0, R_{\text{max}}]$ *prior to* each fit. γ_c, γ_h, and N_g are randomly varied around the values given in Table I, i.e., $\gamma_c \in [0.9, 1.1]$ fm, $\gamma_h \in [1.8, 2.2]$ fm, and $N_g \in [20, 30]$. A_i is optimized as a free parameter using a least-squares fit with χ^2 defined by Eq. (6). The experimental normalization uncertainties for the low and high momentum transfer data sets are taken to be 3% and 2.4% from Refs. [18,27], respectively. To introduce the extended tail constraint with the wave functions in the fits, a few points from the far periphery density distributions calculated from the FC and Hankel wave functions are taken from $r = 6.2$ fm for ^{6}He and from $r = 6.7$ fm for ^{8}He to 12 fm for both nuclei, and added to the data from the experiment. The selections of the starting points are based on the conclusion presented in Ref. [23], that only ≈1% nuclear matter contributes to the overall density distributions at large radii, i.e., at $r > 6.2$ fm for ^{6}He and $r > 6.7$ fm for ^{8}He, and the experimentally deduced ^{6,8}He radii are weakly dependent on the selection of the far periphery density asymptotics. The χ^2 for the quality of the fits is therefore redefined by inserting an additional term, $\sum_i (\frac{\rho_{wf}(r_i)-\rho_{SOG}(r_i)}{\Delta\rho_{wf}(r_i)})^2$ in Eq. (6), where $\rho_{wf}(r_i)$ and $\rho_{SOG}(r_i)$ are the calculated densities using the given wave function, and the SOG fit at the radius r_i. Large uncertainties $\Delta\rho_{wf}(r_i)$ of 30%, are used to allow for only minor contributions from the wave functions to the fits. The probability histograms of the overall χ^2 values for ^{6}He and ^{8}He are presented in the inset of Fig. 4. According to the criterion of having χ^2 smaller than 80 for ^{6}He, and smaller than 120 for ^{8}He, respectively, the good fits for ^{6,8}He are selected and presented as the two bundles of solid lines in Fig. 4. As observed from the figure, the SOG fits reproduce well the overall cross sections at the measured momentum transfer region for both nuclei.

By averaging the radius values corresponding to all these fits presented in Fig. 4 with an equal weight, the point matter rms radii of ^{6,8}He are deduced to be

2.29(6) fm for ^{6}He,
2.53(7) fm for ^{8}He.

The overall errors of the obtained matter rms radii include contributions (a) due to the experimental statistics (0.02 fm for both ^{6}He and ^{8}He), and (b) due to the uncertainties of the SOG fitting procedure including uncertainties of the γ_c, γ_h, R_{c-h}, and N_g randomizations, the uncertainties of the pN scattering amplitude parameters, and the uncertainties of the cross section normalization (0.05 fm for ^{6}He and 0.06 fm for ^{8}He, respectively). The present ^{6,8}He matter radii are compared with those from former analyses using model-dependent density parametrizations [23,28,45] in Table III, where the results from Refs. [23,28] were obtained from analyzing elastic proton scattering data, whereas the results of Ref. [45] were obtained from a combined analysis of the interaction cross sections of ^{4,6,8}He +C reactions, and the neutron removal cross sections of ^{6,8}He +C reactions. It can be found from the table that for both ^{6}He and ^{8}He nuclei, the radii from the present practical model-independent and

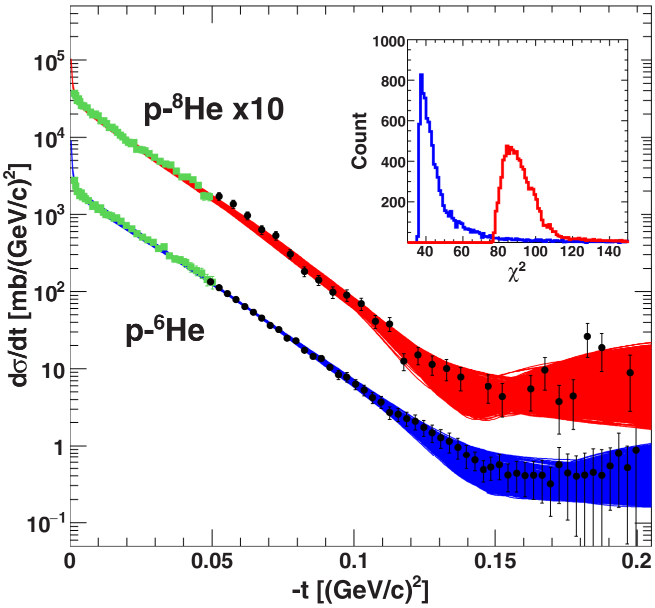

FIG. 4. Measured differential cross sections $d\sigma/dt$ as a function of the four-momentum transfer squared $-t$ for p-^{6}He and p-^{8}He scattering at energies around 700 MeV/u. Green squares represent data measured at low momentum transfer from Ref. [18], and black dots represent data measured at higher momentum transfer from Ref. [27]. The measured differential cross section of p-^{8}He is multiplied by a factor of 10. The bundle of solid lines corresponds to all "good" fits within the framework of the Glauber multiple-scattering theory using SOG distributions for describing the matter densities. The inset shows the probability histograms of the resulting χ^2 values for ^{6}He (in blue) and ^{8}He (in red), respectively.

TABLE III. Point nuclear matter radii R_m for ^{6}He and ^{8}He from the present analysis, compared with results from former model-dependent analyses using different density parametrizations. The point proton radii R_p, the point neutron radii R_n, and the neutron and proton radius difference ΔR_{np} for ^{6}He and ^{8}He are listed in the third to fifth columns. The R_p values are experimentally deduced from the high-precision laser spectroscopy data [2,47]; the R_n values are evaluated from the experimentally deduced R_m and R_p using the relation $R_m^2 = (ZR_p^2 + NR_n^2)/A$; the ΔR_{np} values are evaluated as $\Delta R_{np} = R_n - R_p$.

	R_m (fm)	R_p (fm)	R_n (m)	ΔR_{np} (fm)
^{6}He	2.29(6)	1.925(12) [2,47]	2.45(9)	0.53(9)
	2.30(7) [23]		2.47(10)	0.54(10)
	2.44(7) [28]		2.66(10)	0.74(10)
	2.33(4) [45]		2.51(6)	0.58(6)
^{8}He	2.53(7)	1.807(28) [2,47]	2.73(9)	0.92(10)
	2.45(7) [23]		2.63(9)	0.82(10)
	2.50(8) [28]		2.69(10)	0.88(11)
	2.49(4) [45]		2.68 (5)	0.87(6)

previous model-dependent analyses are in close agreement within errors, demonstrating a weak sensitivity of the matter rms radii on the constraints made in model-dependent analyses for describing the nuclear matter density. No significant difference is found between the radius values deduced from elastic proton scattering data measured at single low momentum transfer [23] and from the combined data at both low and high momentum transfer [28] for both ^{6}He and ^{8}He. This result supports previous theoretical predictions, that proton scattering at low momentum transfer is sensitive to the halo structures appearing at the periphery of nuclei, and from differential cross sections measured with high accuracy at low momentum transfer the overall nuclear size can be determined precisely [23,46].

The present work includes the total matter distributions in ^{6}He and ^{8}He evaluated reliably by the SOG method, while their charge rms radii are deduced with good accuracy from the isotope shift measurement based on high-precision laser spectroscopy [47]. By defolding from the finite size of the proton, the point proton rms radii for ^{6}He and ^{8}He are deduced to be 1.925(12) fm and 1.807(28) fm, respectively [2]. Using the obtained point rms radii of nuclear matter and proton, R_m and R_p, the point neutron rms radii R_n for ^{6}He and ^{8}He are evaluated to be 2.45(9) fm and 2.73(9) fm, respectively, using the relation $R_m^2 = (ZR_p^2 + NR_n^2)/A$, where Z, N, and A are the charge, neutron, and mass numbers for a given nucleus. The differences between neutron and proton radius, $\Delta R_{np} = R_n - R_p$, can be then evaluated to be 0.53(9) fm for ^{6}He and 0.92(10) fm for ^{8}He, respectively. Similarly, R_n and ΔR_{np} are evaluated for the case of model-dependent analyses [23,28,45]. The obtained ΔR_{np} values of ^{6}He and ^{8}He favorably compare to those of the present work (see Table III). The ΔR_{np} values of ^{6,8}He are definitely thicker than those of some heavy nuclei with a large neutron excess (such as $^{116-124}$Sn [48] and $^{204-208}$Pb [6]). This fact is closely related to the weak binding energies of the valence nucleons in ^{6,8}He nuclei. The ^{6}He structure has been well understood to consist of a two-neutron halo outside the α-like core [2,49]. Adding two more neutrons to ^{6}He to obtain ^{8}He results in an even larger value of ΔR_{np} [with a 0.34(10) fm increase], indicating a halo structure, rather than a skin structure [49], existing in ^{8}He as well.

The radial matter density distributions of the ^{6,8}He nuclei deduced in the present analysis are presented with shaded bands representing the uncertainties in Fig. 5. For both neutron-rich ^{6,8}He, extended matter distributions are observed, showing that the matter densities of ^{6,8}He at the nuclear periphery decrease much more slowly with the radius than that of the compact ^{4}He displayed in Fig. 3. Similar results have been also observed in former analyses using phenomenological parametrizations for the description of the density distributions (see Refs. [23,28]). Thus, the present analysis confirms the halo structure in both the ^{6,8}He nuclei. Of particular interest in the present analysis is to compare the radial shapes of the matter distributions of ^{6}He and ^{8}He. Significantly different shapes of the matter density distributions between ^{6}He and ^{8}He are observed around the core region, whereas the densities of ^{6}He and ^{8}He agree within errors with each other in the very central region. The density of ^{8}He in the core region turns out to be with increasing r slightly larger than that of ^{6}He, and up to around 3 fm, both densities coincide again. At even larger radii, the nuclear densities in both

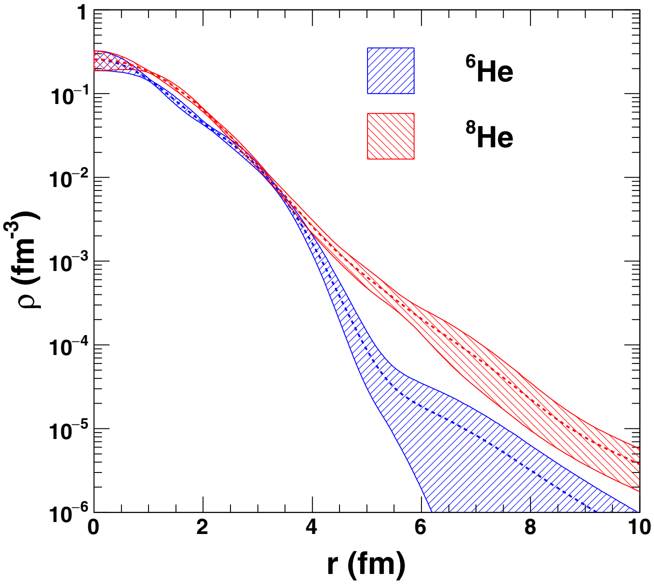

FIG. 5. Point nuclear matter density distributions deduced from the experimental cross sections of p-^{6}He (in blue) and p-^{8}He (in red) elastic scattering using the SOG method. The dashed lines represent the mean distributions deduced; the shaded error bands relate to the errors from the standard deviation.

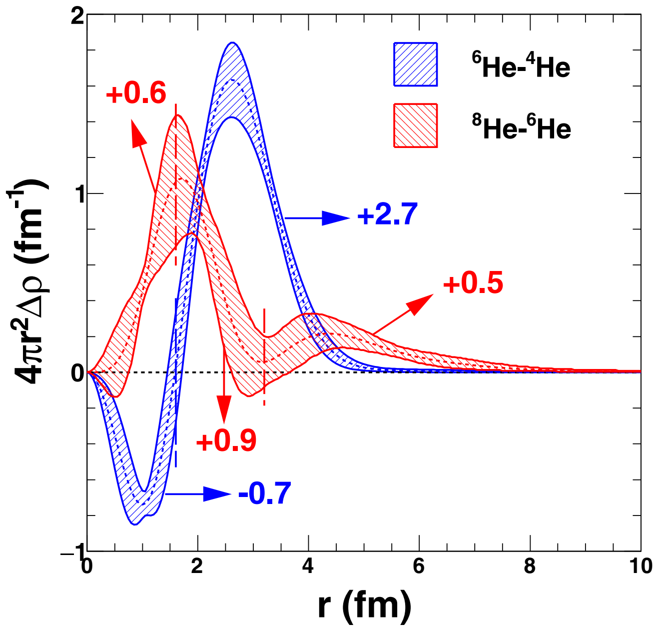

FIG. 6. Differences of the deduced point nuclear matter density distributions between ^{6}He and ^{4}He (in blue) and between ^{8}He and ^{6}He (in red), multiplied with $4\pi r^2$. The dashed lines in the center of the shaded error band represent the mean density difference. The numbers refer to the deficit or the excess of the nucleon number in the integral limits indicated by the vertical dashed lines.

^{6}He and ^{8}He decrease slowly as r increases. As compared to ^{6}He, the density distribution of ^{8}He at large radii is more extended, which is also reflected in the obtained matter radii listed in Table III. It should be pointed out that the density difference between ^{6}He and ^{8}He can be only elucidated in the present work, as on one side, using the SOG analysis allows to deduce the density distributions getting rid of the constraint using the phenomenological parametrizations, and therefore turns out to be less model-dependent, and on the other side, the cross section measurement at high momentum transfer helps to improve the accuracy with which the density at small radii can be deduced.

For providing further insight into the nuclear structure of the ^{6,8}He nuclei, the differences of the deduced point matter density distributions between ^{6}He and ^{4}He, and between ^{8}He and ^{6}He, multiplied with $4\pi r^2$, are plotted in Fig. 6. Pronounced different oscillating structures are observed for the density difference between ^{6}He and ^{4}He, and between ^{8}He and ^{6}He. For ^{6}He, formed by adding two neutrons to ^{4}He, in the region from $r = 0$ fm to the zero crossing at $r = 1.6$ fm, around 0.7 nucleons are found to apparently transfer from the inner core to the further outside surface, and summing up with the two additional nucleons, a plus of 2.7 nucleons is found at $r > 1.6$ fm. This result reflects a significant core rearrangement effect from ^{4}He to ^{6}He by adding two valence neutrons. In contrast, after adding two more valence neutrons to ^{6}He producing ^{8}He, two peaks are exhibited. The peak at small radii strongly indicates a core compensation due to additional two valence neutrons outside. In particular, the integration of the density difference between ^{8}He and ^{6}He from $r = 0$ fm to 1.6 fm results in an increase of about 0.6 nucleons in the average, thus compensating ≈86% of the 0.7 nucleons lost from ^{4}He to ^{6}He in the core region. For completeness, the difference of the point matter density distributions between ^{8}He and ^{4}He is displayed in Fig. 7, and compared with the difference of the point matter density distributions between ^{6}He and ^{4}He (same as that in Fig. 6). It is interesting to note that very similar structures are obtained, indicating a moving of nuclear matter out of the core.

The observed core rearrangement effect by adding the valence neutrons two-by-two outside the $s_{1/2}$ shell closure in ^{4}He finds support from the fact that the experimentally deduced proton radii of ^{6}He and ^{8}He listed in Table III are larger than that of ^{4}He supposed to be the core of ^{6}He and ^{8}He, 1.48(3) fm corresponding to the ^{4}He point matter density distribution displayed in Fig. 3, where the error is calculated following the same way as for the ^{6}He and ^{8}He nuclei. Moreover, the previous model-dependent analyses of the elastic p-^{6,8}He scattering cross sections measured at low momentum transfer [23], and at both low and high momentum transfer [28], using the Gaussian-Gaussian and Gaussian-oscillator density parametrizations which allow us to treat the core and valence nucleons explicitly also indicate a larger α-like core radius in ^{6}He and ^{8}He, supporting the present findings.

Both the behavior of the charge radii and core radii in ^{6}He and ^{8}He, as well as the core rearrangement from ^{4}He to ^{6}He and to ^{8}He observed in the present work (see Figs. 6 and 7), can be well interpreted by a pronounced center-of-mass motion of the core around the center of mass of the whole nucleus [4,23,28,47]. The strength of this effect depends on

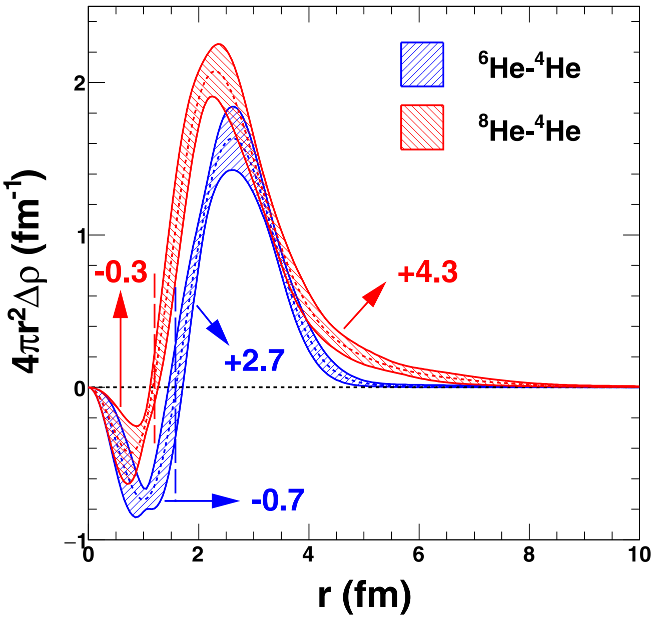

FIG. 7. Same figure as Fig. 6, but for the differences of point nuclear matter density distributions between ^{6}He and ^{4}He (in blue) and between ^{8}He and ^{4}He (in red), multiplied with $4\pi r^2$.

the strength of the correlation between the valence neutrons. This interpretation is well supported by recent *ab initio* calculations (see Ref. [50], and references in Ref. [4]). As for ^{6}He, the recoil motion of the α-like core against the strongly correlated neutron pair smears out the nuclear matter distribution of ^{6}He, leading to the density rearrangement from the core to the outside. After adding two more valence neutrons to form ^{8}He, the four excess neutrons are correlating less and moving more chaotically around the α-like core, so that the recoil of the four neutrons to the α-like core becomes weaker. The weaker recoil effect leads to a weaker smearing-out of the nuclear matter distribution in ^{8}He, and therefore a compensation of the core density occurs. This interpretation is also supported by the findings of Chulkov *et al.* [51] and Papadimitriou *et al.* [52] that ^{8}He is not a closed shell nucleus, and therefore a strong contribution of a ^{6}He $+2n$ configuration is favored. Consequently, compared to that of ^{6}He given by $\alpha + 2n$, the amplitude of the di-neutron configuration in the ground-state wave function of ^{8}He is reduced, demonstrating a more chaotic movement of the valence neutrons in ^{8}He, and therefore, a weaker recoil effect in the center-of-mass coordinate space is expected in ^{8}He. Other evidence for this interpretation is found in the geometrical correlation analyses of the valence neutrons from the experimental ^{6,8}He charge and matter radii [2], where the rms distance from the center of mass of ^{8}He to the center of mass of the valence neutrons is deduced to be 1.07(5) fm, being much smaller than that for ^{6}He, 2.52(5) fm.

Also as shown in Fig. 6, an additional 1.4 nucleons are distributed at $r > 1.6$ fm by adding the two valence neutrons from ^{6}He to ^{8}He. The second peak at large radii shown in the matter density difference between ^{8}He and ^{6}He suggests that in addition to the amount of nucleons transferring toward the core region, there are some of the newly added nucleons (around 0.5 nucleons from the integration at $r > 3.2$ fm) located outside ^{6}He, contributing to the periphery in ^{8}He. As a consequence, ^{8}He shows a large neutron and proton radius difference and a significantly more extended density distribution at the periphery, compared to ^{6}He, resulting in a significant neutron halo in ^{8}He.

IV. SUMMARY

In this article, differential cross sections for elastic p-^{6}He and p-^{8}He scattering at projectile energies around 700 MeV/u, measured in inverse kinematics in the region from low to high momentum transfer up to the first diffraction minimum [$0.002 \leqslant |t| \lesssim 0.2$ (GeV/c)^2] at GSI Darmstadt, are analyzed applying the sum-of-Gaussians (SOG) method based on the Glauber multiple-scattering theory. The rms point matter radii of ^{6}He and ^{8}He are deduced to be 2.29(6) fm and 2.53(7) fm, respectively. The present results are in close agreement with the matter radii of ^{6,8}He deduced from former analyses using phenomenological parametrizations for describing the matter distributions. The application of the SOG method which is, as compared to the previous analyses using phenomenological parametrizations for modeling the nuclear matter distributions, less model-dependent, allows us for the first time to elucidate local characteristics of the overall radial matter densities in both nuclei. In particular, a significant difference in the shapes of density distributions between both nuclei at small radii is exhibited, benefiting from the cross section measurement at high momentum transfer. A pronounced core rearrangement by adding the valence neutrons two-by-two outside an α-like core to form ^{6}He and ^{8}He is obtained. This core rearrangement can be interpreted by the pronounced center-of-mass motion of the α-like core around the center of mass of the ^{6}He or ^{8}He nucleus. The stronger core rearrangement effect in ^{6}He compared to that in ^{8}He can be understood in a way that in ^{6}He, the recoil effect of the two strongly correlated valence neutrons with respect to the α-like core smears out the nuclear matter distribution, whereas, in contrast, for ^{8}He, the spatial distribution of the four valence neutrons is more chaotic, the correlation of the valence neutrons being reduced, and thus the smearing-out effect from the recoil between the core and the valence neutrons is significantly weakened. In addition, more nucleons are found to contribute to the periphery tail of ^{8}He, demonstrating a significant neutron halo in ^{8}He.

ACKNOWLEDGMENTS

We thank the staff of the FRS of GSI, Darmstadt, of the St. Petersburg Nuclear Physics Institute (PNPI), Gatchina, and of the Kurchatov Institute, Moscow, for their great support for taking the experimental data [18,27]. We also thank L. V. Chulkov for his helpful comments and suggestions. This research was supported by the National Natural Science Foundation of China (No. 11705242).

[1] I. Tanihata, H. Hamagaki, O. Hashimoto, Y. Shida, N. Yoshikawa, K. Sugimoto, O. Yamakawa, T. Kobayashi, and N. Takahashi, Phys. Rev. Lett. **55**, 2676 (1985).

[2] I. Tanihata, H. Savajols, and R. Kanungo, Prog. Part. Nucl. Phys. **68**, 215 (2013).

[3] P. Egelhof (for IKAR Collaboration), Prog. Part. Nucl. Phys. **46**, 307 (2001).

[4] Z. T. Lu, P. Mueller, G. W. F. Drake, W. Nörtershäuser, Steven C. Pieper, and Z. C. Yan, Rev. Mod. Phys. **85**, 1383 (2013).

[5] V. Lapoux and N. Alamanos, Eur. Phys. J. A **51**, 91 (2015).

[6] J. Zenihiro, H. Sakaguchi, T. Murakami, M. Yosoi, Y. Yasuda, S. Terashima, Y. Iwao, H. Takeda, M. Itoh, H. P. Yoshida, and M. Uchida, Phys. Rev. C **82**, 044611 (2010).

[7] C. M. Tarbert, D. P. Watts, D. I. Glazier, P. Aguar, J. Ahrens, J. R. M. Annand, H. J. Arends, R. Beck, V. Bekrenev, B. Boillat, A. Braghieri, D. Branford *et al.*, Phys. Rev. Lett. **112**, 242502 (2014).

[8] A. Trzcińska, J. Jastrzębski, P. Lubiński, F. J. Hartmann, R. Schmidt, T. von Egidy, and B. Kłos, Phys. Rev. Lett. **87**, 082501 (2001).

[9] S. Abrahamyan *et al.* (PREX Collaboration), Phys. Rev. Lett. **108**, 112502 (2012).

[10] C. J. Batty, E. Friedman, H. J. Gils, and H. Rebel, Adv. Nucl. Phys. **19**, 1 (1989).

[11] E. T. Boschitz, W. K. Roberts, J. S. Vincent, M. Blecher, K. Gotow, P. C. Gugelot, C. F. Perdrisat, L. W. Swenson, and J. R. Priest, Phys. Rev. C **6**, 457 (1972).

[12] G. D. Alkhazov, S. L. Belostotsky, and A. A. Vorobyov, Phys. Rep. **42**, 89 (1978).

[13] G. D. Alkhazov, S. L. Belostotsky, O. A. Domchenkov, Yu. V. Dotsenko, N. P. Kuropatkin, V. N. Nikulin, M. A. Shuvaev, and A. A. Vorobyov, Nucl. Phys. A **381**, 430 (1982).

[14] A. N. Antonov, D. N. Kadrev, M. K. Gaidarov, E. Moya de Guerra, P. Sarriguren, J. M. Udias, V. K. Lukyanov, E. V. Zemlyanaya, and G. Z. Krumova, Phys. Rev. C **72**, 044307 (2005).

[15] H. Sakaguchi and J. Zenihiro, Prog. Part. Nucl. Phys. **97**, 1 (2017).

[16] P. Egelhof, G. D. Alkhazov, M. N. Andronenko, A. Bauchet, A. V. Dobrovolsky, S. Fritz, G. E. Gavrilov, H. Geissel, C. Gross, A. V. Khanzadeev, G. A. Korolev, G. Kraus, A. A. Lobodenko, G. Münzenberg, M. Mutterer, S. R. Neumaier, T. Schäfer, C. Scheidenberger, D. M. Seliverstov, N. A. Timofeev *et al.*, Eur. Phys. J. A **15**, 27 (2002).

[17] G. D. Alkhazov, M. N. Andronenko, A. V. Dobrovolsky, P. Egelhof, G. E. Gavrilov, H. Geissel, H. Irnich, A. V. Khanzadeev, G. A. Korolev, A. A. Lobodenko, G. Münzenberg, M. Mutterer, S. R. Neumaier, F. Nickel, W. Schwab, D. M. Seliverstov, T. Suzuki, J. P. Theobald, N. A. Timofeev, A. A. Vorobyov *et al.*, Phys. Rev. Lett. **78**, 2313 (1997).

[18] S. R. Neumaier, G. D. Alkhazov, M. N. Andronenko, A. V. Dobrovolsky, P. Egelhof, G. E. Gavrilov, H. Geissel, H. Irnich, A. V. Khanzadeev, G. A. Korolev, A. A. Lobodenko, G. Münzenberg, M. Mutterer, W. Schwab, D. M. Seliverstov, T. Suzuki, N. A. Timofeev, A. A. Vorobyov, and V. I. Yatsoura, Nucl. Phys. A **712**, 247 (2002).

[19] O. A. Kiselev, F. Aksouh, A. Bleile, O. V. Bochkarev, L. V. Chulkov, D. Cortina-Gil, A. V. Dobrovolsky, P. Egelhof, H. Geissel, M. Hellström, N. B. Isaev, B. G. Komkov, M. Matoš, F. V. Moroz, G. Münzenberg, M. Mutterer, V. A. Mylnikov, S. R. Neumaier, V. N. Pribora, D. M. Seliverstov *et al.*, Nucl. Instrum. Methods Phys. Res., Sect. A **641**, 72 (2011).

[20] A. V. Dobrovolsky, G. D. Alkhazov, M. N. Andronenko, A. Bauchet, P. Egelhof, S. Fritz, H. Geissel, C. Gross, A. V. Khanzadeev, G. A. Korolev, G. Kraus, A. A. Lobodenko, G. Münzenberg, M. Mutterer, S. R. Neumaier, T. Schäfer, C. Scheidenberger, D. M. Seliverstov, N. A. Timofeev, A. A. Vorobyov *et al.*, Nucl. Phys. A **766**, 1 (2006).

[21] S. Ilieva, F. Aksouh, G. D. Alkhazov, L. Chulkov, A. V. Dobrovolsky, P. Egelhof, H. Geissel, M. Gorska, A. Inglessi, R. Kanungo, A. V. Khanzadeev, O. A. Kiselev, G. A. Korolev, X. C. Le, Yu. A. Litvinov, C. Nociforo, D. M. Seliverstov, L. O. Sergeev, H. Simon, V. A. Volkov *et al.*, Nucl. Phys. A **875**, 8 (2012).

[22] G. A. Korolev, A. V. Dobrovolsky, A. G. Inglessi, G. D. Alkhazov, P. Egelhof, A. Estradé, I. Dillmann, F. Farinon, H. Geissel, S. Ilieva, Y. Ke, A. V. Khanzadeev, O. A. Kiselev, J. Kurcewicz, X. C. Le, Yu. A. Litvinov, G. E. Petrov, A. Prochazka, C. Scheidenberger, L. O. Sergeev *et al.*, Phys. Lett. B **780**, 200 (2018).

[23] G. D. Alkhazov, A. V. Dobrovolsky, P. Egelhof, H. Geissel, H. Irnich, A. V. Khanzadeev, G. A. Korolev, A. A. Lobodenko, G. Münzenberg, M. Mutterer, S. R. Neumaier, W. Schwab, D. M. Seliverstov, T. Suzuki, and A. A. Vorobyov, Nucl. Phys. A **712**, 269 (2002).

[24] R. J. Glauber, in *Lectures in Theoretical Physics*, edited by W. E. Brittin and L. G. Dunham, Vol. 1 (Interscience, New York, 1959), p. 315.

[25] L. V. Chulkov, C. A. Bertulani, and A. A. Korsheninnikov, Nucl. Phys. A **587**, 291 (1995).

[26] S. Chebotaryov, S. Sakaguchi, T. Uesaka, T. Akieda, Y. Ando, M. Assie, D. Beaumel, N. Chiga, M. Dozono, A. Galindo-Uribarri, B. Heffron, and A. Hirayama, Prog. Theor. Exp. Phys. **2018**, 053D01 (2018).

[27] O. A. Kiselev, F. Aksouh, A. Bleile, O. V. Bochkarev, L. V. Chulkov, D. Cortina-Gil, A. V. Dobrovolsky, P. Egelhof, H. Geissel, M. Hellström, N. B. Isaev, B. G. Komkov, M. Matoš, F. V. Moroz, G. Münzenberg, M. Mutterer, V. A. Mylnikov, S. R. Neumaier, V. N. Pribora, D. M. Seliverstov *et al.*, Eur. Phys. J. A **25**, 215 (2005).

[28] L. X. Chung, O. A. Kiselev, D. T. Khoa, and P. Egelhof, Phys. Rev. C **92**, 034608 (2015).

[29] I. Sick, Nucl. Phys. A **218**, 509 (1974).

[30] X. Liu, P. Egelhof, O. Kiselev, and M. Mutterer, Phys. Lett. B **809**, 135776 (2020).

[31] M. von Schmid *et al.* (Submitted to Nature).

[32] P. Egelhof *et al.* (for EXL Collaboration), JPS Conf. Proc. **6**, 020049 (2015).

[33] M. von Schmid *et al.* (for EXL Collaboration), Phys. Scr. T **166**, 014005 (2015).

[34] H. de Vries, C. W. de Jager, and C. de Vries, At. Data Nucl. Data Tables **36**, 495 (1987).

[35] M. V. Zhukov, B. V. Danilin, D. V. Fedorov, J. M. Bang, I. J. Thompson, and J. S. Vaagen, Phys. Rep. **231**, 151 (1993).

[36] N. Michel, W. Nazarewicz, M. Płoszajczak, and T. Vertse, J. Phys. G **36**, 013101 (2009).

[37] J. S. McCarthy, I. Sick, and R. R. Whitne, Phys. Rev. C **15**, 1396 (1977).

[38] J. S. Al-Khalili and J. A. Tostevin, Phys. Rev. C **57**, 1846 (1998).

[39] J. S. Al-Khalili, J. A. Tostevin, and I. J. Thompson, Phys. Rev. C **54**, 1843 (1996).
[40] P. G. Hansen, Phys. Rev. Lett. **77**, 1016 (1996).
[41] C. Patrignani *et al.* (Particle Data Group), Chin. Phys. C **40**, 100001 (2016).
[42] L. Ray, Phys. Rev. C **20**, 1857 (1979).
[43] O. G. Grebenjuk, A. V. Khanzadeev, G. A. Korolev, S. I. Manayenkov, J. Saudinos, G. N. Velichko, and A. A. Vorobyov, Nucl. Phys. A **500**, 637 (1989).
[44] I. Sick, Phys. Rev. C **77**, 041302(R) (2008).
[45] I. Tanihata, D. Hirata, T. Kobayashi, S. Shimoura, K. Sugimoto, and H. Toki, Phys. Lett. B **289**, 261 (1992).
[46] G. D. Alkhazov and A. A. Lobodenko, Pis'ma Zh. Eksp. Teor. Fiz. **55**, 377 (1992) [JETP Lett. **55**, 379 (1992)].
[47] P. Mueller, I. A. Sulai, A. C. C. Villari, J. A. Alcántara-Núñez, R. Alves-Condé, K. Bailey, G. W. F. Drake, M. Dubois, C. Eléon, G. Gaubert, R. J. Holt, R. V. F. Janssens, N. Lecesne, Z. T. Lu, T. P. O'Connor, M. G. Saint-Laurent, J. C. Thomas, and L. B. Wang, Phys. Rev. Lett. **99**, 252501 (2007).
[48] S. Terashima, H. Sakaguchi, H. Takeda, T. Ishikawa, M. Itoh, T. Kawabata, T. Murakami, M. Uchida, Y. Yasuda, M. Yosoi, J. Zenihiro, H. P. Yoshida, T. Noro, T. Ishida, S. Asaji, and T. Yonemura, Phys. Rev. C **77**, 024317 (2008).
[49] K. Riisager, Phys. Scr. T **152**, 014001 (2013).
[50] S. C. Pieper, Riv. Nuovo Cimento **31**, 709 (2008).
[51] L. V. Chulkov, F. Aksouh, A. Bleile, O. V. Bochkarev, D. Cortina-Gil, A. V. Dobrovolsky, P. Egelhof, H. Geissel, M. Hellström, N. B. Isaev, O. A. Kiselev, B. G. Komkov, M. Matoš, F. V. Moroz, G. Münzenberg, M. Mutterer, V. A. Mylnikov, S. R. Neumaier, V. N. Pribora, D. M. Seliverstov *et al.*, Nucl. Phys. A **759**, 43 (2005).
[52] G. Papadimitriou, A. T. Kruppa, N. Michel, W. Nazarewicz, M. Płoszajczak, and J. Rotureau, Phys. Rev. C **84**, 051304(R) (2011).